Supplementary information

A hole spin qubit in a fin field-effect transistor above 4 kelvin

In the format provided by the authors and unedited

Supplementary Information:
A hole spin qubit in a fin field-effect transistor above 4 kelvin

Leon C. Camenzind,[1, *] Simon Geyer,[1, *] Andreas Fuhrer,[2] Richard J. Warburton,[1] Dominik M. Zumbühl,[1, †] and Andreas V. Kuhlmann[1, 2, †]

[1]*Department of Physics, University of Basel,*
Klingelbergstrasse 82, CH-4056 Basel, Switzerland
[2]*IBM Research-Zürich, Säumerstrasse 4, CH-8803 Rüschlikon, Switzerland*
(Dated: January 4, 2022)

CONTENTS

* These authors contributed equally to this work;
† e-mail: dominik.zumbuhl@unibas.ch, andreas.kuhlmann@unibas.ch

S1.   EXPERIMENTAL SETUP

In this Supplementary section, the measurement setup as well as the pulse scheme are explained in more detail. A schematic of the circuitry to operate and measure the qubits is shown in Fig. S1a. All experiments were performed by measuring hole transport through a double quantum dot (DQD). Pauli spin blockade (PSB) is used for spin-to-charge conversion in order to read out the final qubit state. The qubit operation and readout scheme is illustrated in Fig. S1b.

A BasPI LNHR 927 DAC was used to apply DC voltages to the gate electrodes of the device to form a DQD. The same absolute voltage but of opposite sign is applied to the input of two BasPI LSK389A IV-converters connected to the source and drain contacts of the device. The IV-converters transform the current through the device into voltage signals, which are subtracted with a BasPI SP1002 for common-mode noise rejection to achieve a better signal-to-noise ratio.

A coaxial line with total nominal attenuation of $8\,\mathrm{dB}$ was connected to the sample via a bias-tee on a home-made printed circuit board (PCB) to provide fast pulsing and microwave (MW) signals. Square-wave signals to drive the system from Pauli spin blockade into Coulomb blockade (see Fig. 1d) were generated with a Tektronix AWG5208 arbitrary waveform generator (AWG). A phase- and amplitude-controlled MW signal was generated with a Keysight E8267D vector signal generator (VSG). I and Q inputs were controlled with individual channels of the AWG. The square-wave and MW signals were combined with a Mini-Circuits ZC2PD-5R264-S+ signal combiner. The output of a Signal Recovery 7265 lock-in amplifier was connected to the pulse modulation (PM) input of the VSG to chop the MW signal at a frequency of $89.17\,\mathrm{Hz}$. The transport signal from the sample was demodulated with the lock-in amplifier and digitised with a National Instruments USB-6363 data acquisition device (DAQ).

In Fig. S1b we show the three stages of the pulse scheme which are used to initialise (I), manipulate (M) and read out (R) the qubits. Note that the initialisation and readout stage are nominally identical. The qubit is initialised in a situation where the (1,1) and (0,2) charge states are only slightly detuned (see schematic (I) in Fig. S1b). If a spin-up hole tunnels into the left dot, it can tunnel to the right dot and form a singlet with the spin-down hole of the right dot. Subsequently, it leaves the system and thermalises with the right reservoir. However, if a spin-down hole tunnels into the left dot, the transition into the singlet state is forbidden due to the Pauli exclusion principle. In principle the hole could tunnel to the right dot and form a triplet state, but in practice the hole lacks the energy to occupy an excited orbital state, a necessary step to form a triplet. Therefore, the spin state blocks the hole from tunnelling. The probability that a spin-up or spin-down hole tunnels into the system at the beginning of the cycle is equal.

After the initialisation stage, the left hole is in the spin ground state, denoted $|\downarrow\rangle$, as indicated by the orange arrow on the Bloch sphere sketched in Fig. S1b. Here, we will discuss the manipulation of the hole spin residing in the left quantum dot (left qubit), but the same discussion is valid for the hole in the right dot since initialisation and readout are only sensitive to the possibility of the two spins forming a singlet. For simplicity, we use a rotating wave description.

Following initialisation, the system is pulsed into Coulomb blockade, such that the holes cannot tunnel out of the dot during manipulation. During this manipulation stage, a MW signal is applied to the left plunger gate (see Fig. 1b). If the frequency of the MW signal matches the magnetic-field-induced spin splitting, the spin is rotated on the Bloch sphere due to electric dipole spin resonance (EDSR). The spin rotates around the x-axis for a time $t_{\rm b}$ during which the MW signal is applied. This results in Rabi oscillations between $|\downarrow\rangle$ and $|\uparrow\rangle$ (purple data in Fig. S1b). Note that the x-axis of the Bloch sphere is defined by the phase of the MW signal as soon as the first pulse is applied. A rotation around the y-axis is achieved by changing the phase of the MW signal by $\pi/2$.

After the manipulation stage, the qubit is read out in the same energy configuration as in the initialisation stage: if the left and the right dots have opposite spin and can form a singlet, a hole is allowed to tunnel out of the DQD. If the pulse sequence is repeated fast, these tunnelling events result in a measurable current which is proportional to the probability of the left spin to be in $|\uparrow\rangle$ after (M), assuming the right spin is in the $|\downarrow\rangle$ state. The maximum current expected upon completely lifting PSB (π_x-pulse) is $I_{max} = e\Gamma$ where Γ is the repetition rate of the pulse cycle and e the elementary charge. In our lock-in measurement scheme, we measure the difference in current when MW are applied and the qubit is operated, and when the MW are not applied and the qubit remains in PSB. This allows us to distinguish the current due to the pulse sequence from background leakage current. In the example shown in Fig. S1b, $I_{max} \sim 200\,{\rm fA}$ was found. This agrees very well with the expectation for a total pulse cycle of $800\,{\rm ns}$ ($\Gamma = 1.25\,{\rm MHz}$) used for this measurement. This method only allows us to determine the statistical average of events and does not allow for single-shot readout.

This transport-based readout requires a high repetition rate ($\sim 1\,{\rm MHz}$), such that our signal can be distinguished from the noise. Therefore the duration of the manipulation stage is limited and hence the number of gate operations in a randomised benchmarking experiment (see Fig. 3) or decoupling pulses in a CPMG experiment (see Fig. 4) is limited. This limitation becomes more severe as temperature increases, since the readout contrast degrades (see Supplementary Note S8).
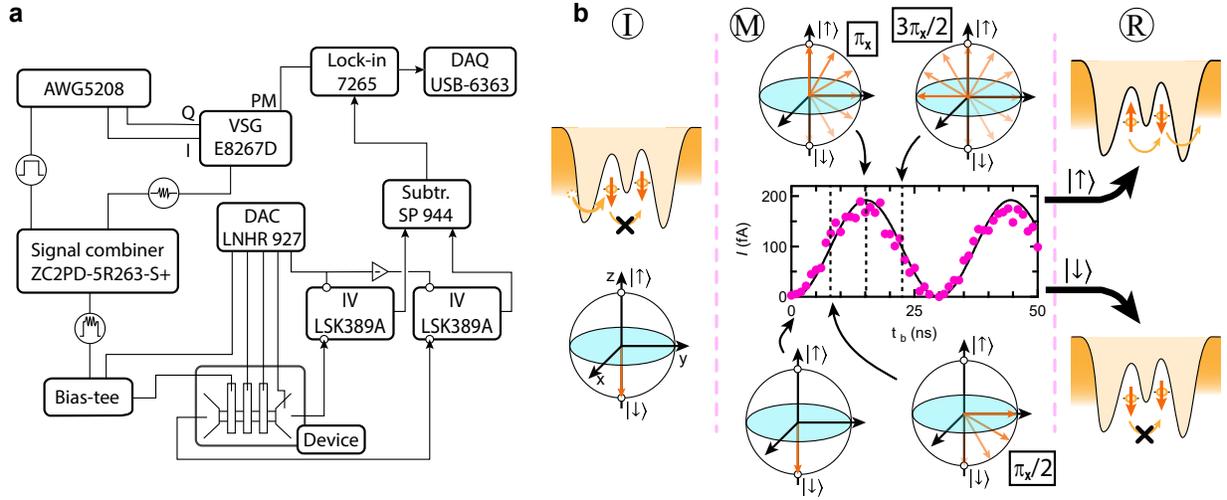
FIG. S1. **Experimental setup and measurement scheme. a** Schematic circuit of the measurement and control electronics. **b** Pulse scheme for the left qubit: the DQD cartoon illustrates hole transport, while the Bloch sphere visualises the state of the spin-1/2 qubit. (I) Due to PSB, the qubit is initialised in the ground state which we here assume to be $|\downarrow\rangle$. (M) Rabi oscillations are driven between $|\downarrow\rangle$ and $|\uparrow\rangle$ states. The Bloch spheres show the qubit state after different burst times t_b. For $t_b = 15.2$ ns, for example, the spin is flipped, which corresponds to a π_x-pulse. (R) The spin state is projected onto the z-axis in a spin-to-charge conversion scheme. Transport through the reservoir via the right quantum dot is only possible if the final state is $|\uparrow\rangle$. When this scheme is repeated fast enough, a current proportional to the $|\uparrow\rangle$ probability of the left spin is measured.

S2. QUANTUM DOT OCCUPANCIES

Our transport-based measurement scheme does not allow us to determine the exact hole occupation number. In Fig. S2a the first observable pairs of bias triangles are shown. Even at a high source-drain voltage of $V_{SD} = 100\,\text{mV}$ no additional bias triangles appear (see Fig. S2c). PSB is observed for the two pairs of bias triangles indicated by the blue and green dot for opposite bias direction. We assign these triangles to (1,1) - (0,2)/(2,0) charge transitions. Here, (m, n) denotes the effective number of holes in the DQD, while the absolute number of holes in the DQD is $(m + m_0, n + n_0)$.

We were able to form and operate qubits at both transitions and found similar operation speeds as well as coherence times. In this work, we only discuss the qubits energised and measured at the green transition.
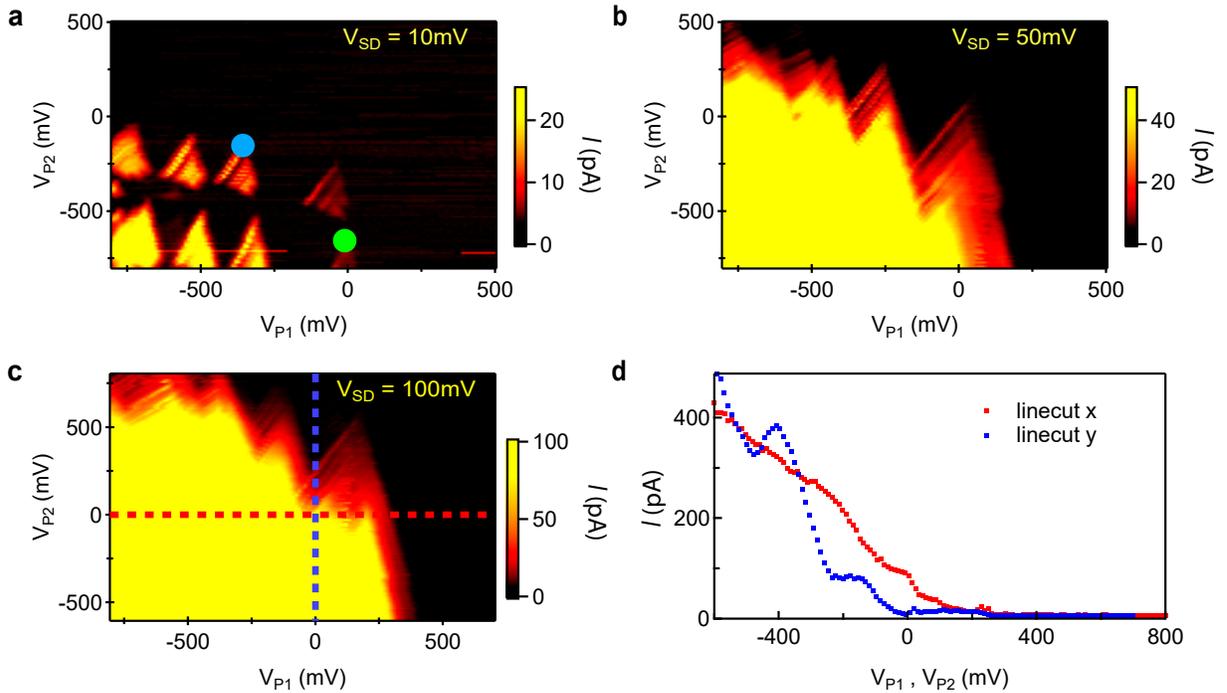

FIG. S2. **Double dot charge occupation.** Charge stability diagrams for $V_{SD} = 10\,\text{mV}$ **a**, $V_{SD} = 50\,\text{mV}$ **b** and $V_{SD} = 100\,\text{mV}$ **c**. No additional bias triangles become visible when increasing V_{SD} from $10\,\text{mV}$ to $100\,\text{mV}$. The line-cuts in **d** are taken along the indicated lines in **c**. The blue and green dot in **a** indicate the transition showing spin blockade for opposite bias direction. The qubits discussed in the main text were energised at the green transition.

S3. MICROWAVE POWER CALIBRATION

The attenuation of the MW signal from the MW signal generator to the qubit is a function of frequency, caused by e.g. impedance mismatches and resonances due to the PCB or bonding wires. Therefore, the MW power that arrives at the qubit has to be calibrated. Because the Rabi frequency f_{Rabi} depends on the MW power (see Fig. 1i), this calibration is necessary to compare the Rabi frequency at different Larmor frequencies.

To calibrate the MW power, the qubit's response to a continuous wave excitation is measured. In the limit of a large dot-reservoir tunnel coupling in comparison to the MW signal frequency [1, 2], the $(1,1) - (0,2)$ charge transition at the baseline of the bias-triangle (see inset of Fig. S3, Fig. S7a and Fig. 1c) is broadened by the MW power due to photon-assisted tunnelling (PAT). The broadening $\Delta\varepsilon$ is measured along the detuning axis and then converted into a voltage $eA_{\mathrm{MW}} = \Delta\varepsilon$ which drops over the inter-dot tunnel barrier [3] (see Fig. S3). This broadening of the transition depends on the MW signal that effectively arrives at the qubit. Therefore, the measured MW amplitude A_{MW} permits a calibration and thus a comparison of the Rabi frequency at different Larmor frequencies for the same driving strength A_{MW} (see Fig. 1i).

The calibrated voltage amplitude A_{MW} allows us to estimate the electric field $|E_{\mathrm{MW}}|$ at the QDs, necessary in order to estimate the spin-orbit length l_{SO} (see Supplementary Note S7).
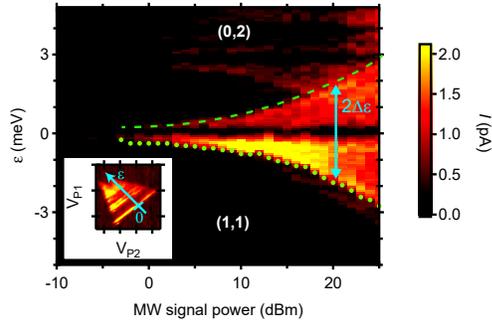

FIG. S3. **Example of calibrating $A_{\mathbf{MW}}$.** Due to a capacitive coupling to the QD, the zero-detuning line is broadened upon applying a MW signal on the left plunger gate P1. This broadening $2\Delta\varepsilon$ (blue) allows A_{MW} to be calculated. A_{MW} is the MW-induced voltage drop over the inter-dot tunnel barrier as $eA_{\mathrm{MW}} = \Delta\varepsilon$. A larger amplitude, here given as the power of the MW signal at the signal generator output, results in an increase of the transition broadening $\Delta\varepsilon$. The green data points are values of $\Delta\varepsilon$ extracted using a signal threshold algorithm. The inset shows the bias triangle and the axis used to define the detuning ε (blue axis).

S4. RABI AND RAMSEY EXPERIMENTS AT DIFFERENT TEMPERATURES

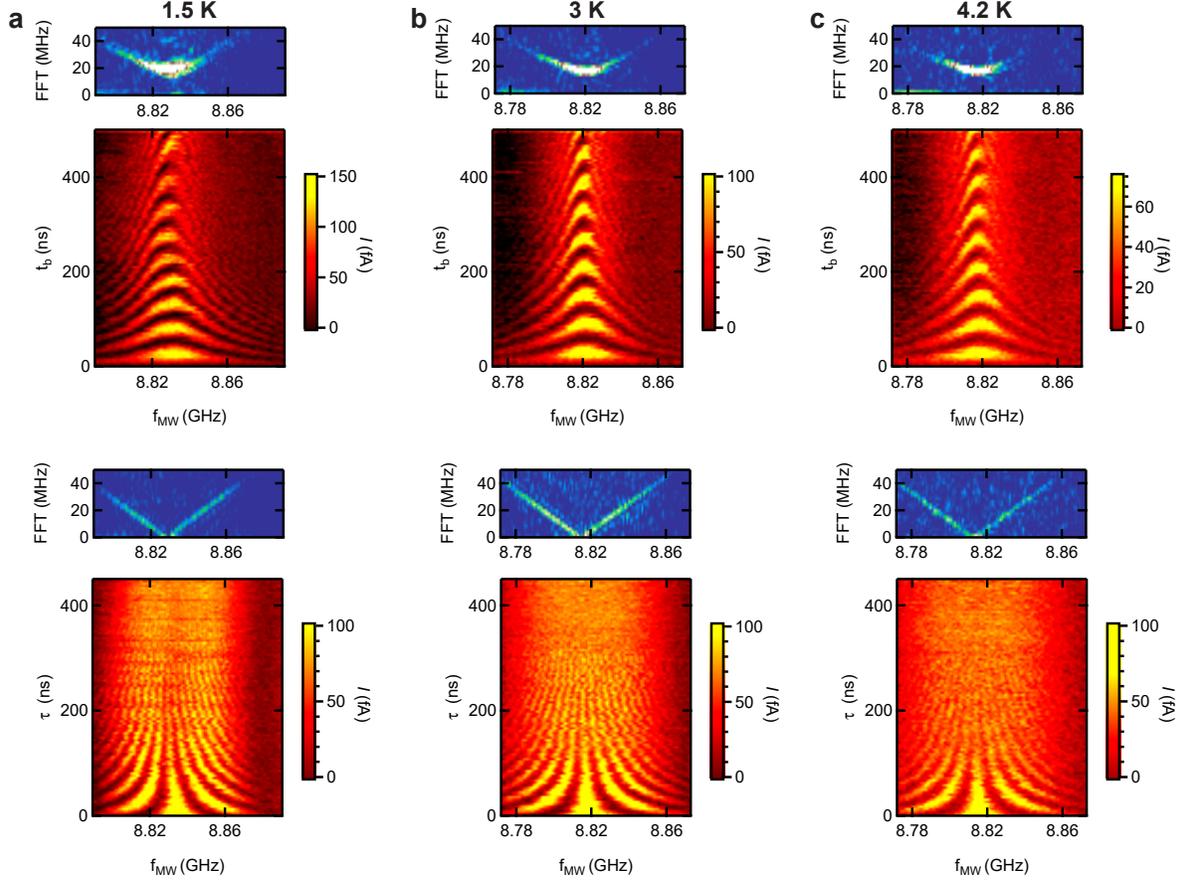In Fig. S4 we show Rabi and Ramsey measurements at T = 1.5, 3 and 4.2 K.

FIG. S4. **Coherent qubit control at different temperatures.** Comparison of Rabi chevron patterns and Ramsey fringes at **a** 1.5, **b** 3 and **c** 4.2 K for Q2. The FFTs show the quadratic dependence of f_{Rabi} on the frequency detuning in the Rabi measurements and a linear dependence on the frequency detuning in the Ramsey experiments.

S5.   FAST RABI OSCILLATIONS

Hole spin qubits allow for fast all-electrical spin rotations. In our experiments, we observed Rabi frequencies as high as $f_{\text{Rabi}} = 147\,\text{MHz}$ for Q1.
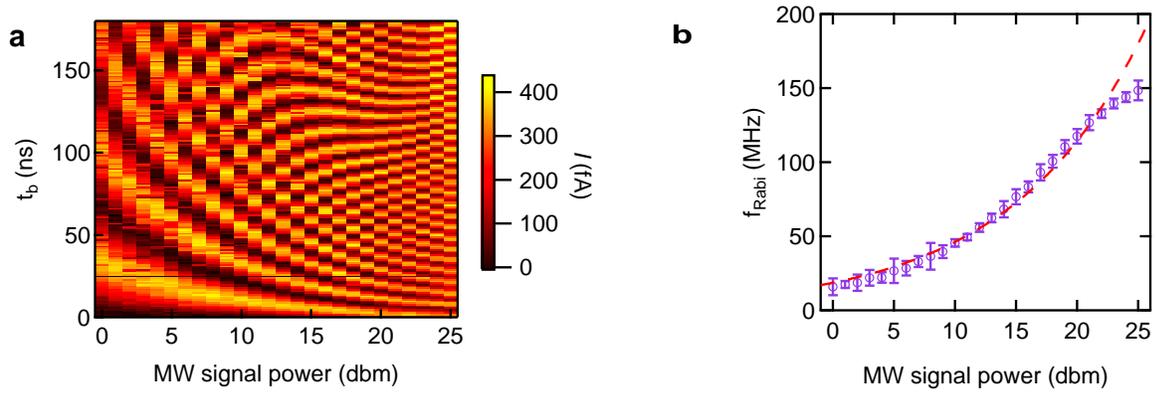

FIG. S5. **Fast Rabi oscillations a** Rabi oscillations at $T = 1.5\,\text{K}$ and $f_{\text{L}} \sim 8\,\text{GHz}$ as a function of MW signal power. **b** The Rabi frequency extracted by a FFT-analysis of the data in **a** shows the maximum $f_{\text{Rabi}} = 147\,\text{MHz}$ at $25\,\text{dbm}$. f_{Rabi} follows a square-root dependence on the the MW signal power at the VS output (red dashed line). The MW signal power is quadratically related to the calibrated MW voltage A_{MW}. Therefore, this dependence agrees very well with the linear dependence of f_{Rabi} on A_{MW} in Fig. 1i. The observed saturation at higher power could be an indication of an anharmonic confinement potential [2, 4, 5].

S6.   ESTIMATE OF EFFECTIVE DOT SIZES

In this section we estimate the effective dot size. We assign Q1/Q2 to the left/right QD, i.e. Q1 is closer to the MW drive applied to the left plunger gate P1. This assignment is based on the fact that Q1 has the higher Rabi frequency f_{Rabi} and larger g-factor tunability with the square pulse amplitude A_{p} (see Fig. 1g).

The effective dot size can be estimated by $l_{\mathrm{dot}} = \hbar/\sqrt{(m^*\Delta)}$, where m^* denotes the effective mass and Δ the orbital energy. Assuming a weak exchange interaction, Δ is given by the single-dot singlet-triplet splitting Δ_{ST}, such that $\Delta_{\mathrm{Q1}} = 5.3\,\mathrm{meV}$ and $\Delta_{\mathrm{Q2}} = 3.3\,\mathrm{meV}$. Ref. [6] states values for the effective mass for holes in silicon nanowires ranging from $0.184\,m_0$ to $0.794\,m_0$, depending on the nanowire orientation. Since the exact shape and orientation of our hole wavefunction is unknown, and also strain is neglected in Ref. [6], we assume an average effective mass of $m^* = 0.45\,m_0$ to extract $l_{\mathrm{dot}}^{\mathrm{Q1}} \approx 6\,\mathrm{nm}$ and $l_{\mathrm{dot}}^{\mathrm{Q2}} \approx 7\,\mathrm{nm}$. The estimated size of the QDs compare well with the plunger gate length of $\sim 15\,\mathrm{nm}$.

S7. ESTIMATE OF SPIN-ORBIT LENGTH

The strength of the spin-orbit interaction can be characterised by the spin-orbit length l_{SO}, where $\pi l_{SO}/2$ describes the distance a hole has to be displaced to induce a spin-orbit mediated spin flip. We estimate l_{SO} using the following equation for spin-orbit mediated EDSR [1, 7]:

$$l_{SO} = \frac{g\mu_B}{2hf_{Rabi}} \left(2|B_{ext}| \frac{\hbar^2}{\Delta^2 m^*} e|E_{MW}| \right), \tag{1}$$

where B_{ext} denotes the external magnetic field, Δ the orbital energy of the QD hosting the qubit, $|E_{MW}|$ the electric field strength of the MW driving field, m^* the effective mass of the charge carrier and g is the Landé g-factor in the direction of B_{ext}. Here, we assume that EDSR is driven by a periodic displacement of the wave function as a whole without modulating the spin splitting (sometimes referred to as iso-Zeeman EDSR [8]). We use an effective mass $m^* = 0.45 m_0$ (see Supplementary Note S6).

To estimate the electric field strength $|E_{MW}|$ at the location of the qubits, the MW amplitude A_{MW} extracted from PAT measurements is used (see Supplementary Note S3). A_{MW} drops across the inter-dot tunnel barrier, which we estimate by the distance between the two QDs $d_{dd} \sim 45 - 60$ nm (see Fig. 1b) [3]. Consequently, $|E_{MW}^{Q1}| = A_{MW}/d_{dd}$ is the electric field in Q1, the qubit below gate P1. We assume that $|E_{MW}^{Q2}|$ is smaller than $|E_{MW}^{Q1}|$ by a factor of 4 (for $d_{dd} = 45$ nm) to 6 (for $d_{dd} = 60$ nm) due to its larger distance to P1 ($\sim 45 - 60$ nm for Q2 in comparison to ~ 10 nm for Q1).

In Fig. S6a,b we show l_{SO} extracted for different MW signal amplitudes A_{MW} for Q1 (red) and Q2 (blue) using the data from Fig. 1i. From this data we estimate an average $l_{SO} \sim 20 - 60$ nm. Using $E_{SO} = \hbar^2/(2m^* l_{SO}^2)$, l_{SO} can be converted into a spin-orbit energy $E_{SO} \sim 30 - 150 \,\mu$eV (see Fig. S6c,d) which is in good agreement with theoretical predictions for a Si nanowire with rectangular cross section of diameter $4 - 10$ nm (green box) [6].
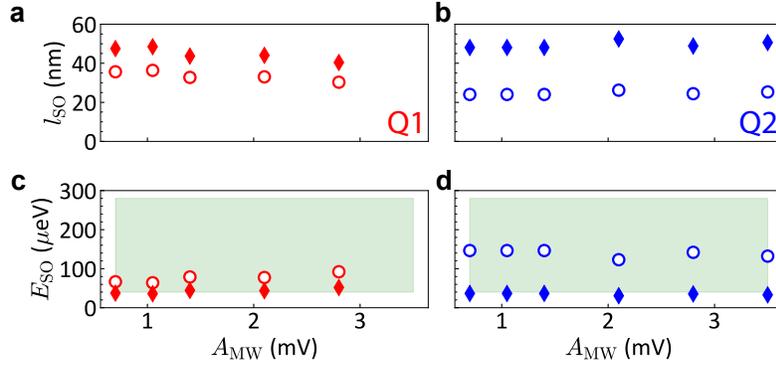
FIG. S6. **Spin-orbit length.** Estimated spin-orbit length l_{SO} using the data from Fig. 1i for **a** Q1 (red) and **b** Q2 (blue). A distance $d_{dd} = 45\,\text{nm}$ (60 nm) and a ratio of $E_{\text{MW}}^{\text{Q1}}/E_{\text{MW}}^{\text{Q2}} = 4$ (6) was used for the data depicted as diamonds (circles). **c,d** Spin-orbit energy E_{SO} corresponding to l_{SO} from **a** and **b**. The data is in good agreement with the theoretical prediction (green box) [6].

S8.   TEMPERATURE DEPENDENCE OF PAULI SPIN BLOCKADE

In this section we discuss the temperature dependence of the Pauli spin blockade, which is closely linked to the temperature dependence of our qubit readout. Spin blockade is revealed by a suppression of current flow through the base of the bias triangles at $B_{\mathrm{ext}} = 0\,\mathrm{T}$, as shown in Fig. S7a. A finite magnetic field B_{ext} lifts PSB and a leakage current is observed (see Fig. S7b). The presence of a zero-field dip is an indication that lifting of PSB is dominated by spin-orbit interaction [9]. Note that the dip is offset from $B_{\mathrm{ext}} = 0\,\mathrm{T}$ due to trapped flux in the magnet.

Fig. S7c shows line-cuts of the leakage current along B_{ext} at $\varepsilon = 0$ for temperatures in the range of 1.5 to 14 K. The dips, that can be observed up to $\sim 12\,\mathrm{K}$, are well fitted by a Lorentzian function [9]. To characterise the efficiency of PSB we plot the dip amplitude A_{PSB} as a function of temperature T in Fig. S7d (left axis, purple data). We find that A_{PSB} shows a Gaussian decay with T.

Since our qubit readout scheme relies on PSB, we compare the PSB efficiency with our temperature-dependent qubit readout signal. In Fig. S7d the qubit readout current $I(t_b = t_\pi)$ after applying a π-pulse is shown for temperatures from 1.5 to 6.5 K (right axis, yellow and red data). I shows a stronger exponential decay with temperature than the Gaussian decay observed for A_{PSB}, such that the qubit readout only works up to $\sim 6\,\mathrm{K}$. When comparing the decay of A_{PSB} and I, one has to take into account that EDSR experiments were performed at $B_{\mathrm{ext}} > 50\,\mathrm{mT}$. Therefore, A_{PSB} and I might have a different sensitivity to T.

PSB is protected against temperature by the single dot singlet-triplet splitting $\Delta_{\mathrm{Q1}} = 5.3\,\mathrm{meV}$ and $\Delta_{\mathrm{Q2}} = 3.3\,\mathrm{meV}$. Spin-flip cotunnelling experiences a strong thermal smearing of $5.4\,k_B T$ [10], such that the extracted orbital energies correspond to temperatures of 11 K and 7 K. This analysis suggests that the suppression of PSB with increasing temperature is in good agreement with spin-flip cotunnelling.
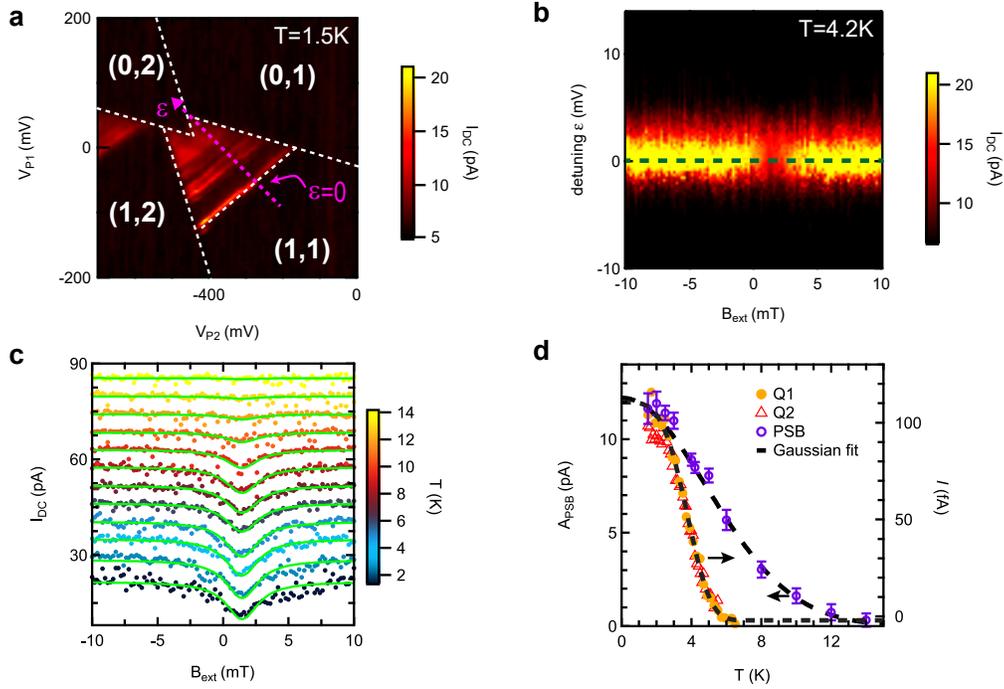
FIG. S7. **Spin blockade temperature dependence. a** Pair of bias triangles with detuning axis (pink arrow) at $V_{\mathrm{SD}} = 12\,\mathrm{mV}$. **b** Spin blockade leakage current as a function of magnetic field and detuning. Close to zero magnetic field the current is strongly suppressed, indicating Pauli spin blockade. In presence of spin-orbit interaction, spin blockade is lifted by applying a finite magnetic field. The dip offset from $B_{\mathrm{ext}} = 0\,\mathrm{T}$ is due to trapped flux in our magnet. **c** Line cuts along B_{ext} at $\varepsilon = 0$ at T = 1.5 to 14 K. The spin blockade efficiency decreases with increasing temperature, which is seen from the decay of the dip amplitude. **d** T-dependence of PSB efficiency A_{PSB} extracted from Lorentzian fits from the cuts in **c** (left axis, purple points). The data fit well to a Gaussian function $A_{\mathrm{PSB}} \propto \exp\left(-(T/T_A)^2\right)$ with width $T_A \approx 6.9 \pm 0.2\,\mathrm{K}$. The decay of the Rabi signals in both qubits (yellow/red symbols), on the other hand, shows a stronger temperature dependence and fits well to $I \propto \exp\left(-(T/T_I)^\gamma\right)$ with $\gamma \approx 4 \pm 0.2$ and $T_I \approx 4.1 \pm 0.1$.

S9.   EDSR SPECTRAL LINEWIDTH

We confirm the T_2^* temperature dependence presented in Fig. 2d by measuring the EDSR linewidth in a continuous-wave experiment. In this measurement, the qubit was pulsed into Coulomb blockade and a continuous MW signal was applied to drive the spin. The power of the MW signal was carefully chosen to avoid power-broadening. A set of data for Q2 at $f_L \sim 8.8\,\mathrm{GHz}$ is shown Fig. S8 for temperatures up to 6 K. A Gaussian function is fitted to the resonance to determine the full width at half maximum Δf_{FWHM}. The coherence time T_2^* is related to Δf_{FWHM} by [11, 12]

$$T_2^* = \frac{2\sqrt{\ln 2}}{\pi \cdot \Delta f_{\mathrm{FWHM}}}. \tag{2}$$

In Fig. S8b the extracted temperature dependence of T_2^* is presented. The results from this continuous-wave experiment are in agreement with the pulsed experiments shown in Fig. 2b-d.
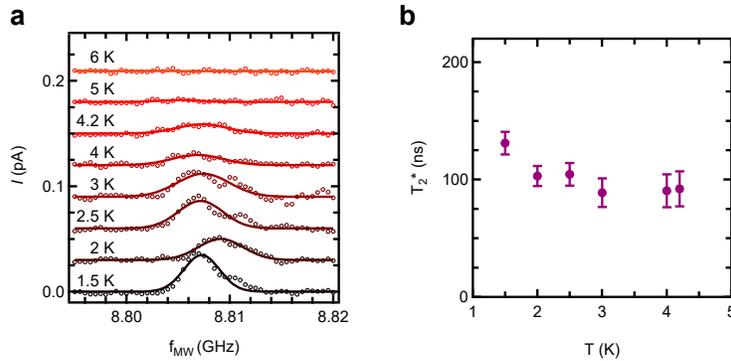

FIG. S8. T_2^* **temperature dependence extracted from EDSR linewidth measurements. a** Response of Q2 to a continuous-wave excitation at $f_L \sim 8.8\,\mathrm{GHz}$ for different temperatures. Close to the spin resonance condition, spin blockade is lifted and a current is detected. The width of the peak is related to the coherence time T_2^* by Eq. 2. **b** Extracted T_2^* from the data shown in **a**.

S10.   LONGEST DEPHASING TIME T_2^*

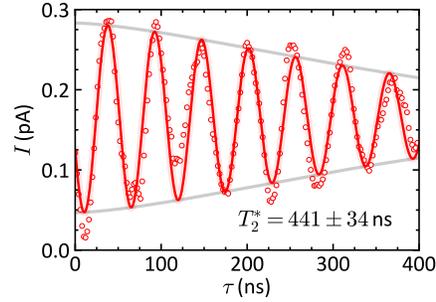In Fig. S9 we show Ramsey fringes of Q2 with a decay time of $T_2^* = 441 \pm 34$ ns.

FIG. S9. **Ramsey experiment demonstrating a long coherence time.** A $T_2^* = 441\pm34$ ns was obtained at $f_L = 5.85$ GHz and T $= 1.5$ K for Q2. The data were taken on resonance with a τ-dependent phase $\phi(\tau)$, which adds an artificial oscillation [13]. The solid curve shows a fit to $A + B\sin(\omega\tau + \theta)\exp\left[-(\tau/T_2^*)^{\beta+1}\right]$ using β from Fig. 4c.

S11. HYPERFINE LIMIT OF T_2^*

In natural silicon there are 4.7% ^{29}Si spin-carrying isotopes present which will lead to dephasing of the qubit. In this section, we give an estimation of the dephasing time T_2^* limited by the finite hyperfine interaction due to the presence of these nuclear spins in the Si host material.

The maximum Overhauser field A experienced by an electron (e) in natural silicon is $A_e = 1.85\,\text{mT}$ [14]. Here, A corresponds to the field if all nuclear spins are polarised. For holes, the hyperfine interaction has been found to be about an order of magnitude weaker [15–18]. Thus, we assume $A_h \sim 0.185\,\text{mT}$. The random Overhauser field fluctuations δA_h are given by

$$\delta A_h = A_h/\sqrt{N_S}, \tag{3}$$

where N_S is the number of non-zero nuclear spins inside the wave function of the QD [19]. The spin coherence time is then

$$T_2^* = \frac{\hbar\sqrt{N_S}}{g\mu_B A_h}. \tag{4}$$

where g is the hole spin g-factor, μ_B is the Bohr magneton and $\hbar$ is the reduced Planck constant.

In order to estimate N_S, we need to calculate the volume of the QD. We assume a cylindrical hole wave function, elongated along the fin and with a diameter of $d \sim 5\,\text{nm}$. For the dimension along the fin, we use the dimensions extracted from the singlet-triplet splitting: $l_{\text{Q1}} = 5.7\,\text{nm}$ and $l_{\text{Q2}} = 7.1\,\text{nm}$ (see also Supplementary Note S7). For the density of silicon $\sim 50\,\text{atoms/nm}^3$ and 4.7% spin carrying ^{29}Si atoms, we find $N_S \sim 280$ ($N_S \sim 350$) in the left (right) QD.

Using the g-factors extracted from EDSR measurements (see Fig. 1f), we find $T_2^* \sim 520\,\text{ns}$ for Q1 and $T_2^* \sim 490\,\text{ns}$ for Q2. The expected increase in coherence for holes in comparison to electron spin qubits [12] due to a smaller A_h is counteracted by our much smaller silicon hole spin qubits and thus a lower N_S. However, while for electrons in Si the hyperfine interaction is isotropic, it is anisotropic for holes. Therefore, we note that the estimated limit for T_2^* corresponds to the worst case scenario in terms of magnetic field orientation [16].

Strikingly, these estimates match rather well with the longest T_2^* found in our experiments, see Supplementary Note S10. This indicates that the residual nuclear spins of the host material may play an important role in limiting the coherence also for hole spin qubits. Furthermore, we estimate an increase to $T_2^* \sim 11\,\mu s$ ($\sim 4\,\mu s$) when the qubit is hosted in an isotropically purified ^{28}Si layer with 100 ppm (800 ppm) residual nuclear spins. These coherence times are comparable to the coherence of state-of-the-art electron spin qubits in isotopically enriched Si using micromagnets [20], but the electron spin qubits still lack behind in operation speed in comparison to their hole counterparts.

S12. SPIN RELAXATION TIME T_1

In Fig. S10 we present an attempt to measure T_1 for Q2 at T $= 4\,$K and $f_L = 7.7\,$GHz. The longest waiting time that could be applied was $1\,\mu$s. Guides to the eye show the expected decay curves for $T_1 = 1$, 3, 6 and $10\,\mu$s. The data suggest a spin relaxation time T_1 longer than $10\,\mu$s. Since T_1 is much longer than our measurement cycles, spin relaxation has no influence on our results. The observed relaxation rate is in good agreement with other experiments and theory [21, 22].
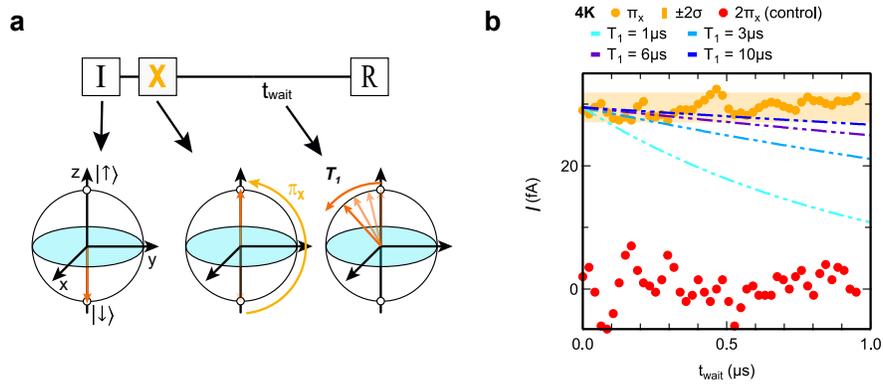

FIG. S10. **Spin relaxation. a** Qubit manipulation scheme to measure spin relaxation: after initialisation in the spin ground state $|\downarrow\rangle$, a π_x pulse brings the qubit into the spin excited state $|\uparrow\rangle$. On a timescale given by the spin relaxation time T_1, the spin polarisation decays from $|\uparrow\rangle$ to $|\downarrow\rangle$. After a waiting time t_{wait}, the residual polarisation $P_{|\uparrow\rangle}$ is measured. This polarisation is expected to show an exponential decay according to $P_{|\uparrow\rangle} \propto e^{-t_{\text{wait}}/T_1}$. **b** Orange data points shows the measurement results for Q2 at T $= 4\,$K and $f_L = 7.7\,$GHz. No T_1-decay is observed for the maximum waiting time of $t_{\text{wait}} = 1\,\mu$s. Guides to the eye, showing the decay curves for $T_1 = 1, 3, 6$ and $10\,\mu$s, indicate $T_1 > 10\,\mu$s. The yellow shaded region shows the two-sigma uncertainty of the measured data. A control measurement with a $2\pi_x$ pulse (red data) instead of the π_x-gate shows that the current after a full 2π spin rotation becomes minimal as expected. The larger noise on the red data is due to a shorter integration time.

S13.   COHERENCE-LIMITED QUALITY FACTOR

We show the dependence of the qubit quality on the MW signal power at 1.5 and 4.2 K. Because of limits on the maximal pulsing time impose by our read-out method, we could not observe T_2^{Rabi} in this experiment. Instead of the driven quality-factor $Q = T_2^{\mathrm{Rabi}} \cdot 2f_{\mathrm{Rabi}}$, we therefore investigate a coherence-limited quality factor Q^* which we define as

$$Q^* = T_2^* \cdot 2f_{\mathrm{Rabi}} = T_2^*/t_\pi \tag{5}$$

where t_π is the spin-flip time.

The data in Fig. S11 were taken for Q2 at $f_L = 8.8\,\mathrm{GHz}$, the same configuration as discussed in Fig. 2. As expected for a power-independent T_2^*, Q^* shows a roughly linear dependence on A_{MW} (see Supplementary Note S3) due to a linear increase of f_{Rabi} on A_{MW} (see Fig. 1i).
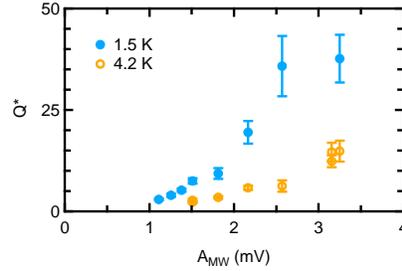

FIG. S11. **Coherence-limited quality factor** $Q^* = T_2^* \cdot 2f_{\mathrm{Rabi}}$ as a function of power at 1.5 and 4.2 K. These data were recorded on Q2 at $f_L = 8.8\,\mathrm{GHz}$. The increase of Q^* with driving amplitude A_{MW} is due to faster Rabi oscillations and thus a shorter spin-flip time t_π.

S14. DYNAMICAL DECOUPLING

In this section, we compare the extended coherence time from dynamical decoupling of Q2 for different numbers of decoupling pulses and temperatures. The measurements presented in Fig. S12 show the normalised difference ΔI of the readout current measured after a projection of the qubit into $|\uparrow\rangle$ and $|\downarrow\rangle$. Ideally, if there is no free evolution of the qubit ($\tau = 0$), $\Delta I(\text{normalised}) = 1$ because the normalised current after projecting into $|\downarrow\rangle = 0$ and $|\uparrow\rangle = 1$. Due to decoherence, the signal decays with increasing τ on a time scale given by the coherence time T_2^* (Ramsey), T_2^{Hahn} (Hahn-echo), or T_2^{CPMG} (CPMG), depending on the pulsing scheme applied. We investigate the free induction decay (Ramsey), one decoupling pulse $n = 1$ (Hahn-echo) and $n = 2, 4, 8, 16$ and 32 decoupling pulses (CPMG-n). Schematics of the pulse sequences are shown at the top of Fig. S12. Note that τ is defined as the free evolution time and thus equals the total time no gate is applied to the qubit. The generally observed decrease of the readout signal with higher temperatures (see Fig. S7) was partially compensated by using shorter pulse cycles (and thus shorter maximal τ). As a consequence, the maximal τ differs for the different traces. In particular for the 4.2 K data, the signal was only measurable for a comparably short maximal $\tau \sim 1\,\mu s$.

For the Ramsey and Hahn-echo experiment, the signal of the full rotation of the second $\pi_\phi/2$ pulse was measured (from $\phi = 0$ to 2π) [23]. The CPMG signal amplitude ΔI was obtained by measuring the difference in current between $\phi = 0$ and $\phi = \pi$, which corresponds to projection onto $|\uparrow\rangle$ and $|\downarrow\rangle$, respectively. These data are used to extract CPMG-n coherence times in Fig. 4a and β in Fig. 4c for 1.5 and 3 K.
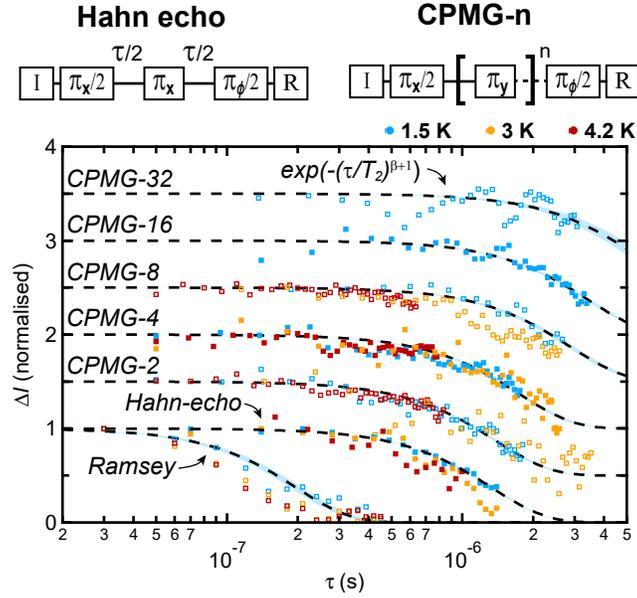
FIG. S12. **Active noise decoupling**. Decoupling of Q2 at $f_L = 8.8\,\text{GHz}$ from low-frequency noise using Hahn-echo and CPMG-n decoupling schemes for $1.5\,\text{K}$ (blue), $3\,\text{K}$ (orange) and $4.2\,\text{K}$ (red). This data was fitted to $\propto \exp\left(-\left(\tau/T_2\right)^{\beta+1}\right)$ (dashed curves) as discussed in the main text. β was obtained by iteratively fitting the decays to extract $T_2^{\text{CPMG-n}}$ and fitting a power-law to the $T_2^{\text{CPMG-n}}$ to extract β [24], as described in Fig. 4a. The obtained CPMG coherence times are summarised in Fig. 4a and the extracted β in Fig. 4c for 1.5 and $3\,\text{K}$. Due to low signal-to-noise which only allowed for a short $\tau \sim 1\mu s$, it was not possible to reliably extract β from the data set at T = $4.2\,\text{K}$.

[1] K. C. Nowack, F. H. L. Koppens, Y. V. Nazarov, and L. M. K. Vandersypen, Coherent Control of a Single Electron Spin with Electric Fields, Science **318**, 1430 (2007).

[2] F. N. M. Froning, L. C. Camenzind, O. A. H. van der Molen, A. Li, E. P. A. M. Bakkers, D. M. Zumbühl, and F. R. Braakman, Ultrafast hole spin qubit with gate-tunable spin–orbit switch functionality, Nature Nanotechnology 10.1038/s41565-020-00828-6 (2021).

[3] S. Nadj-Perge, S. M. Frolov, E. P. A. M. Bakkers, and L. P. Kouwenhoven, Spin–orbit qubit in a semiconductor nanowire, Nature **468**, 1084 (2010).

[4] J. Yoneda, T. Otsuka, T. Nakajima, T. Takakura, T. Obata, M. Pioro-Ladrière, H. Lu, C. Palmstrøm, A. Gossard, and S. Tarucha, Fast Electrical Control of Single Electron Spins in Quantum Dots with Vanishing Influence from Nuclear Spins, Physical Review Letters **113**, 267601 (2014).

[5] K. Takeda, J. Kamioka, T. Otsuka, J. Yoneda, T. Nakajima, M. R. Delbecq, S. Amaha, G. Allison, T. Kodera, S. Oda, and S. Tarucha, A fault-tolerant addressable spin qubit in a natural silicon quantum dot, Science Advances **2**, e1600694 (2016).

[6] C. Kloeffel, M. J. Rančić, and D. Loss, Direct Rashba spin-orbit interaction in Si and Ge nanowires with different growth directions, Physical Review B **97**, 235422 (2018).

[7] V. N. Golovach, M. Borhani, and D. Loss, Electric-dipole-induced spin resonance in quantum dots, Physical Review B **74**, 165319 (2006).

[8] A. Crippa, R. Maurand, L. Bourdet, D. Kotekar-Patil, A. Amisse, X. Jehl, M. Sanquer, R. Laviéville, H. Bohuslavskyi, L. Hutin, S. Barraud, M. Vinet, Y.-M. Niquet, and S. D. Franceschi, Electrical Spin Driving by g -Matrix Modulation in Spin-Orbit Qubits, Physical Review Letters **120**, 137702 (2018).

[9] J. Danon and Y. V. Nazarov, Pauli spin blockade in the presence of strong spin-orbit coupling, Physical Review B **80**, 041301 (2009).

[10] A. Kogan, S. Amasha, D. Goldhaber-Gordon, G. Granger, M. A. Kastner, and H. Shtrikman, Measurements of kondo and spin splitting in single-electron transistors, Physical Review Letters **93**, 166602 (2004).

[11] R. Hanson, L. P. Kouwenhoven, J. R. Petta, S. Tarucha, and L. M. K. Vandersypen, Spins in few-electron quantum dots, Reviews of Modern Physics **79**, 1217 (2007).

[12] E. Kawakami, P. Scarlino, D. R. Ward, F. R. Braakman, D. E. Savage, M. G. Lagally, M. Friesen, S. N. Coppersmith, M. A. Eriksson, and L. M. K. Vandersypen, Electrical control of a long-lived spin qubit in a Si/SiGe quantum dot, Nature Nanotechnology **9**, 666 (2014).

[13] T. F. Watson, S. G. J. Philips, E. Kawakami, D. R. Ward, P. Scarlino, M. Veldhorst, D. E. Savage, M. G. Lagally, M. Friesen, S. N. Coppersmith, M. A. Eriksson, and L. M. K. Vandersypen, A programmable two-qubit quantum processor in silicon, Nature **555**, 633 (2018).

[14] L. V. C. Assali, H. M. Petrilli, R. B. Capaz, B. Koiller, X. Hu, and S. D. Sarma, Hyperfine interactions in silicon quantum dots, Physical Review B **83**, 165301 (2011).

[15] V. S. Pribiag, S. Nadj-Perge, S. M. Frolov, J. W. G. van den Berg, I. van Weperen, S. R. Plissard, E. P. A. M. Bakkers, and L. P. Kouwenhoven, Electrical control of single hole spins in nanowire quantum dots, Nature Nanotechnology **8**, 170 (2013).

[16] J. H. Prechtel, A. V. Kuhlmann, J. Houel, A. Ludwig, S. R. Valentin, A. D. Wieck, and R. J. Warburton, Decoupling a hole spin qubit from the nuclear spins, Nature Materials **15**, 981 (2016).

[17] P. Fallahi, S. T. Yılmaz, and A. Imamoğlu, Measurement of a Heavy-Hole Hyperfine Interaction in InGaAs Quantum Dots Using Resonance Fluorescence, Physical Review Letters **105**, 257402 (2010).

[18] B. Voisin, R. Maurand, S. Barraud, M. Vinet, X. Jehl, M. Sanquer, J. Renard, and S. D. Franceschi,

Electrical control of g-factor in a few-hole silicon nanowire MOSFET, Nano Letters **16**, 88 (2015).

[19] A. V. Khaetskii, D. Loss, and L. Glazman, Electron Spin Decoherence in Quantum Dots due to Interaction with Nuclei, Physical Review Letters **88**, 186802 (2002).

[20] J. Yoneda, K. Takeda, T. Otsuka, T. Nakajima, M. R. Delbecq, G. Allison, T. Honda, T. Kodera, S. Oda, Y. Hoshi, N. Usami, K. M. Itoh, and S. Tarucha, A quantum-dot spin qubit with coherence limited by charge noise and fidelity higher than 99.9%, Nature Nanotechnology **13**, 102 (2017).

[21] A. Crippa, R. Ezzouch, A. Aprá, A. Amisse, R. Laviéville, L. Hutin, B. Bertrand, M. Vinet, M. Urdampilleta, T. Meunier, M. Sanquer, X. Jehl, R. Maurand, and S. D. Franceschi, Gate-reflectometry dispersive readout and coherent control of a spin qubit in silicon, Nature Communications **10**, 10.1038/s41467-019-10848-z (2019).

[22] J. Li, B. Venitucci, and Y.-M. Niquet, Hole-phonon interactions in quantum dots: Effects of phonon confinement and encapsulation materials on spin-orbit qubits, Physical Review B **102**, 075415 (2020).

[23] R. Maurand, X. Jehl, D. Kotekar-Patil, A. Corna, H. Bohuslavskyi, R. Laviéville, L. Hutin, S. Barraud, M. Vinet, M. Sanquer, and S. D. Franceschi, A CMOS silicon spin qubit, Nature Communications **7**, 13575 (2016).

[24] J. Medford, Ł. Cywiński, C. Barthel, C. M. Marcus, M. P. Hanson, and A. C. Gossard, Scaling of Dynamical Decoupling for Spin Qubits, Physical Review Letters **108**, 086802 (2012).